Vis-NIR luminescent lanthanide-doped core-shell nanoparticles for imaging and photodynamic therapy

Ivana Miletto[a], Chiara Gionco[b], Maria Cristina Paganini[b], Simona Martinotti[a], Elia Ranzato[a], Elio Giamello[b], Leonardo Marchese[a] and Enrica Gianotti[a]**

Dr. Ivana Miletto, Dr. Simona Martinotti, Dr. Elia Ranzato, Prof. Leonardo Marchese, Prof. Enrica Gianotti
Department of Science and Technological Innovation, University of Eastern Piedmont "Amedeo Avogadro", Viale Teresa Michel 11, 15121 Alessandria (ITALY)
E-mail: ivana.miletto@uniupo.it, enrica.gianotti@uniupo.it

Dr. Chiara Gionco, Prof. Maria Cristina Paganini, Prof. Elio Giamello
Department of Chemistry, University of Turin, Via Pietro Giuria 9, 10125 Turin (ITALY)

Keywords: lanthanide doped nanoparticles, core-shell nanoparticles, photodynamic therapy, EPR, visible and NIR fluorescence

Abstract

The preparation of smart Ln:ZrO_2@SiO_2 nanoplatforms with grafted photosensitizer (Rose Bengal) which couple optical imaging with photo-dynamic therapy (PDT) is presented. A careful control of the lanthanide dopant loading is considered to enhance the photoemission properties of the lanthanide ions (Er, Pr, Yb) inside the ZrO_2 crystal structure. The nanosystem with the lowest lanthanide loading maintains the size, phase and morphology of pristine ZrO_2 nanoparticles and exhibit the best performances in term of the overall luminescence properties. Upon functionalization with a silica shell to covalently bound Rose Bengal, a theranostic platform is prepared which is very efficient in singlet oxygen generation, as demonstrated by EPR and UV-Vis spectroscopy studies. Preliminary cell viability tests show that while both pristine and Ln doped ZrO_2 nanoparticles do not exert cytotoxicity, neither upon illumination nor in dark condition, Rose Bengal grafted samples are able to significantly reduce cell viability under light exposure, thus confirming the high potential of these nanoparticles as PDT tools.

1. Introduction

In recent years there has been a continuous growth in the design and engineering of multifunctional nanomaterials to be used in medicine as theranostic platforms. Luminescent lanthanide (Ln^{3+})-doped inorganic nanoparticles (LNPs) are emerging as a new class of bioprobes and as an alternative to conventional molecular probes such as lanthanide chelates and organic dyes.[1-3] LNPs have attracted growing attention for their potential applications in different areas such as biodetection, bioimaging, and theranostics, owing to their superior physicochemical features such as long luminescence (from several to tens of milliseconds) lifetime, narrow emission bands, high chemical stability, high resistance to photobleaching, and low toxicity.[4-7] Compared to fluoride NPs ($NaYF_4$ and $NaGdF_4$), that have received great attention due to their upconversion properties,[8] Ln-doped inorganic oxide NPs are considered highly promising as a new and huge family of luminescent bioprobes for their photostability and chemical and thermal stability due to their more rigid crystalline environment and higher lattice binding energy. Beside biocompatible inorganic oxides, zirconium oxide (ZrO_2) is considered an excellent material for optical applications due to its wide bandgap, good transparency, high refractive index and low phonon energy (470 cm^{-1}) and can be an ideal host for Ln^{3+} ions to achieve long-lived Ln luminescence.[9,10] The presence of Ln^{3+} ions into the ZrO_2 matrix allows to modulate the emission properties towards the “first biological window” (650-950 nm) [11] and more interesting towards the “second biological window” (1000-1500 nm). In this latter NIR range, the light offers deeper penetration, reduced optical scattering [12] with respect to both the first biological window and the visible region, and diminished auto-fluorescence. Beside the emission features in a suitable NIR region, it is important to couple other functionalities in order to have therapeutic agents and to develop an efficient theranostic nano-platforms. To introduce an additional chemical functionality, it is necessary to change the hydrophobicity of LNPs surface. Among various methods, the growth of a silica shell on LNPs (LNP@SiO_2) has attracted great interest since SiO_2 exhibits low cytotoxicity and its surface

can be easily modified to introduce various functional groups (−COOH, $-NH_2$, −SH, etc.) via silanization, which can satisfy various needs of conjugating biological molecules or functional nanoparticles.[13,14] A smart design of LNP@SiO_2 nanoplatforms with different kinds of functionalities will enable the development of multifunctional nanomedical platforms coupling biosensing, multimodal bioimaging, drug delivery or photo-dynamic therapy (PDT).[15]

Herein we report the development of luminescent lanthanide-doped core shell (LNP@SiO_2) nanoparticles functionalized with Rose Bengal (RB), a type II photosensitizer (PS), to couple optical imaging with PDT. The different steps of the synthetic procedures and the physico-chemical properties of the LNP@SiO_2RB have been deeply investigated to evidence the emission properties in the Vis-NIR range due to lanthanide ions together with the PDT efficiency of RB. Er, Yb and Pr(III) ions have been inserted separately, with different loadings, in the ZrO_2 nanoparticles. A careful control of the rare earth ions loadings into the ZrO_2 network is extremely important due to the possible ZrO_2 structure modification inferred by the doping ions insertion; for this reason, different lanthanide ions loadings have been explored. To covalently attach the RB, LNPs have been modified with a silica shell containing amino-groups that are necessary to bind covalently RB. Among the large variety of organic dyes, halogen-xanthene dyes, such as Rose Bengal, are well known as PS due to their intense absorption bands in the green region of the visible spectrum (480–550 nm) and high yield in the generation of singlet oxygen. In particular, RB is notable for its high triplet quantum yield ($\Phi_T = 0.76$), fairly long lived triplet state ($t_{1/2}$ = 0.1–0.3 ms), and high singlet oxygen quantum yield ($\Phi\ ^1O_2 = 0.75$ under 540 nm light irradiation).[16-18] The RB loading has been chosen considering some previous studies in order to avoid RB aggregation. [19,20] The singlet oxygen release ability of the RB grafted samples was evaluated by indirect scavenger-assisted UV-Vis and EPR methods. Furthermore, preliminary cell viability tests were carried out in order to test the potential cytotoxicity of lanthanide doped ZrO_2 nanoparticles as such and after functionalization and the PDT ability of the RB grafted samples.

2. Results and Discussion

2.1. Characterization of lanthanide-doped ZrO_2 nanoparticles

Zirconium dioxide nanoparticles doped with different rare-earth ions (Ln:ZrO_2) were successfully prepared by following a simple hydrothermal procedure that uses Zr oxychloride and lanthanide nitrates as precursors. Er^{3+}, Pr^{3+} and Yb^{3+} ions were chosen as dopants and three doping-loadings were investigated for each Ln:ZrO_2 system. In **Table 1**, acronyms, sample composition and loading of dopant ions of the synthesized nanoparticles are reported. The actual loading of lanthanide dopants was checked by EDX (Energy Dispersive X-ray) analysis, confirming that the desired stoichiometry was achieved (see **table S1** and **figure S1**).

Table 1 Acronyms and lanthanide loading of the doped ZrO_2 nanoparticles

Sample composition	**Acronyms**		
	Lanthanide loading *		
	1%	**2%**	**10%**
Er:ZrO_2	EZ1	EZ2	EZ10
Pr:ZrO_2	PZ1	PZ2	PZ10
Yb:ZrO_2	YZ1	YZ2	YZ10

* dopant concentration is expressed as: [Ln/(Ln+Zr)]x100

In order to investigate the effect of the lanthanide ion incorporation on the phase composition of the ZrO_2 matrix, XRD patterns were acquired for the pure and the doped ZrO_2 samples (**Figure 1**). To determine the crystallite size and the relative abundance of phases, Rietveld refinement was performed on the experimental patterns using the MAUD software [21]; the results, reported in **table S2**, allowed us to assign the present phases to tetragonal and monoclinic.[22] The diffraction pattern of the pure ZrO_2 matrix (curve a) obtained with this synthetic method is therefore a mixture of monoclinic (m-ZrO_2, reflections labelled with full circles in figure 1) and tetragonal (t-ZrO_2, reflections labelled with full triangles in figure 1) phases. Irrespective of the Ln^{3+} ion, along with the increase in the loading, the tetragonal phase

is favoured with respect to the monoclinic one and the highest loading samples (10%, curves d) are mainly constituted by t-ZrO_2.

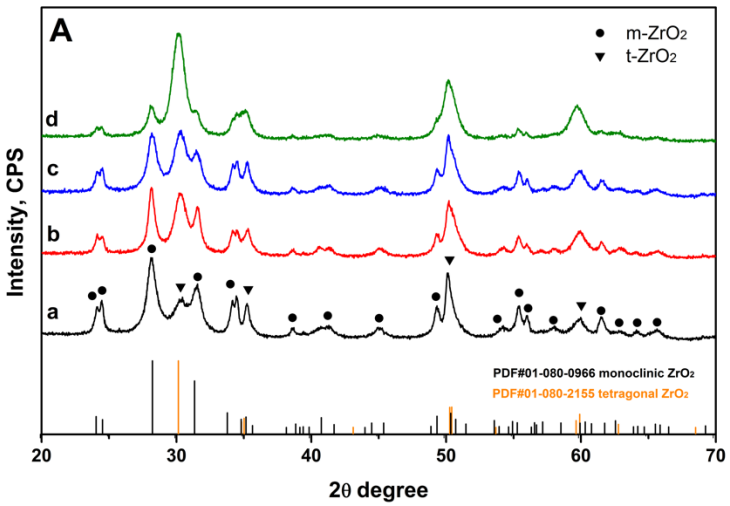

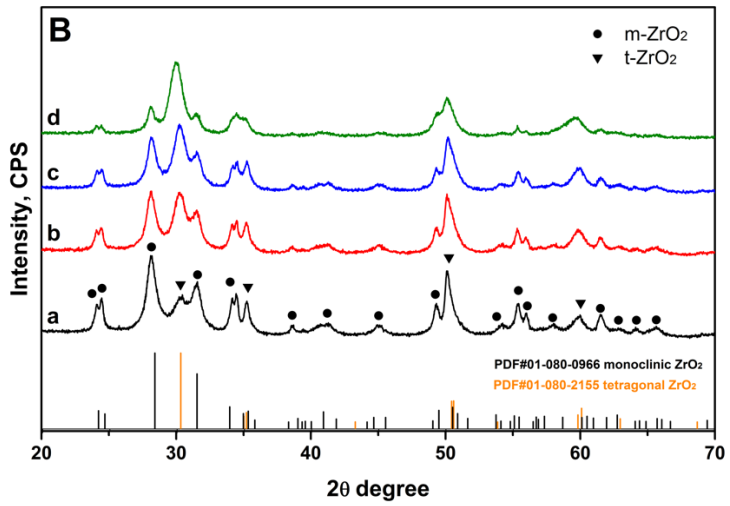

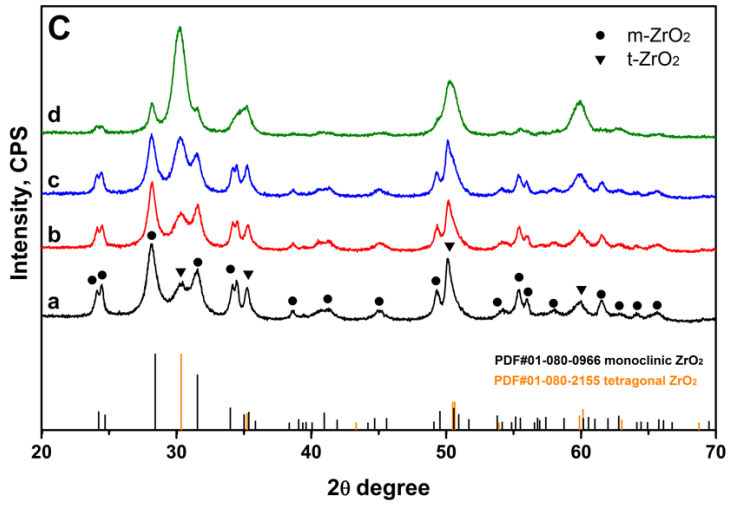

Figure 1 XRD patterns of (a) pure ZrO_2 and Ln-doped ZrO_2, where Ln= Er (section **A**), Pr (section **B**) or Yb (section **C**), at increasing dopant concentrations: (b) 1%; (c) 2% and (d) 10%. Reflections typical of m-ZrO_2 and t-ZrO_2 are labelled with full circles and full triangles respectively and reference patterns of monoclinic and tetragonal ZrO_2 are reported.

The width of the diffracted peaks assigned to the m-ZrO_2 is not constant with the angle of diffraction for all samples, indicating a certain anisotropy in the crystallite dimensions,[23] as confirmed by the values of maximum (D) and minimum (d) crystallite sizes obtained from the Rietveld refinement along the [110] and [-111] plans, respectively (**table S2** and **figure S2**). Hence, the m-ZrO_2 crystallites cannot be considered as "nanospheres" but are more likely characterized by an elliptic shape, as confirmed by TEM imaging (**Figure S3**, supplementary information). Both pure ZrO_2 and Ln:ZrO_2 samples are mainly constituted of anisotropic monoclinic phase crystallites (ca. 50x20 nm); furthermore, some smaller particles, typical of tetragonal phase, are also present.

The pristine nanoparticles are well dispersed in ethanol (**Table S3**, supplementary information) as evidenced by Dynamic Light Scattering (DLS) measurements.

The effect of the lanthanide ion concentration on the optical properties of the ZrO_2 nanoparticles was investigated by Diffuse reflectance (DR) UV-Vis-NIR spectroscopy (**Figure 2**). All spectra are dominated in the UV region by ZrO_2 band-gap transition at 250 nm that is not significantly affected by the presence of lanthanide dopants. The weak absorption around 300 nm due to the presence of point defect in the material slightly increases with the dopant loading.[22,23]

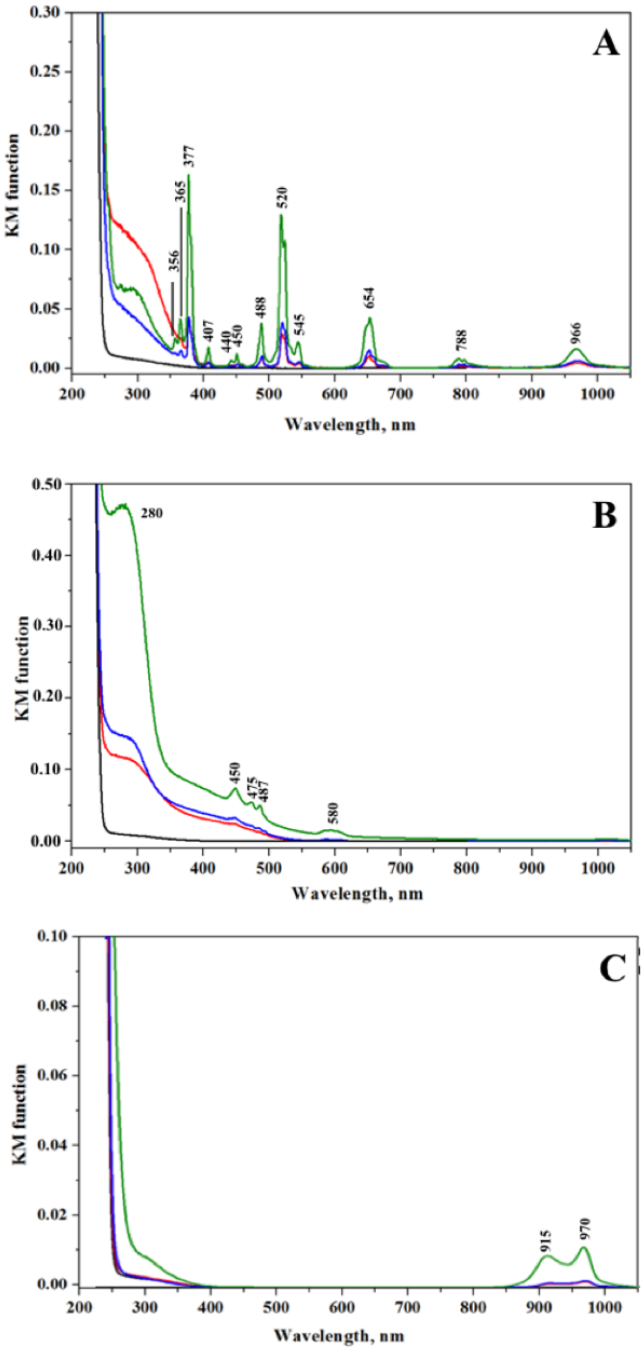

Figure 2 DR UV-Vis spectra of pure ZrO_2 (black curve) and Ln-doped ZrO_2, where Ln= Er (panel **A**), Pr (panel **B**) or Yb (panel **C**), at increasing dopant concentrations: 1% (red curve); 2% (blue curve) and 10% (green curve)

In the visible region, the intensity of the complex set of absorption bands typical of the lanthanides f-f transitions, increases along with the dopant loading. The presence of these complex patterns of bands suggests that dopant ions are well diluted in the ZrO_2 matrix and

preserve their electronic properties, even in the samples at the highest loading. The positions and the corresponding f-f transitions of Er, Pr and Yb ions are reported in **Table 2**. [24,25]

Table 2 Assignment of the Er^{3+}, Pr^{3+} and Yb^{3+} transitions observed in DR UV-Vis-NIR spectra

Ln^{3+} ion	λ_{abs} [nm]	f-f transitions
Er^{3+}	356	$^4I_{15/2} \rightarrow {}^2G_{7/2}$
	365	$^4I_{15/2} \rightarrow {}^2K_{15/2} + {}^4I_{15/2} \rightarrow {}^4G_{9/2}$
	377	$^4I_{15/2} \rightarrow {}^4G_{11/2}$
	407	$^4I_{15/2} \rightarrow {}^2H_{9/2}$
	440	$^4I_{15/2} \rightarrow {}^4F_{3/2}$
	450	$^4I_{15/2} \rightarrow {}^4F_{5/2}$
	488	$^4I_{15/2} \rightarrow {}^4F_{7/2}$
	520	$^4I_{15/2} \rightarrow {}^2H_{11/2}$
	545	$^4I_{15/2} \rightarrow {}^4S_{3/2}$
	654	$^4I_{15/2} \rightarrow {}^4F_{9/2}$
	788	$^4I_{15/2} \rightarrow {}^4I_{5/2}$
	966	$^4I_{15/2} \rightarrow {}^4I_{11/2}$
Pr^{3+}	280	$^3H_4 \rightarrow {}^1S_0$
	450	$^3H_4 \rightarrow {}^3P_2$
	475	$^3H_4 \rightarrow {}^3P_1 + {}^3H_4 \rightarrow {}^1I_6$
	487	$^3H_4 \rightarrow {}^3P_0$
	580	$^3H_4 \rightarrow {}^1D_2$
Yb^{3+}	915	$^2F_{7/2} \rightarrow {}^2F_{5/2}$
	970	$^2F_{7/2} \rightarrow {}^2F_{5/2}$

The visible and NIR emission spectra of all the samples are reported in **Figure 3** and the positions and the corresponding f-f emissions of Er, Pr and Yb ions are reported in **Table 3**. In order to select the more efficient excitation wavelength, emission spectra were measured upon excitation at the different absorption maxima identified from the DR UV-Vis spectra. For all samples, a rapid decrease in luminescence intensity occurs along with the increase dopant loading, due to the concentration quenching effects. [26,27] Pr^{3+} ions excited from the ground state $^3H_4$ to the $^3P_2$ level, relax non-radiatively to the metastable $^3P_0$ state. The $^1D_2$ state can be populated due to cross-relaxation or multiphonon non-radiative relaxation from $^3P_0$ while the $^3P_1$ state is thermally populated. As a consequence, emission from all these levels are possible, and result in bands both in the visible and in the NIR region of the spectra.[28]

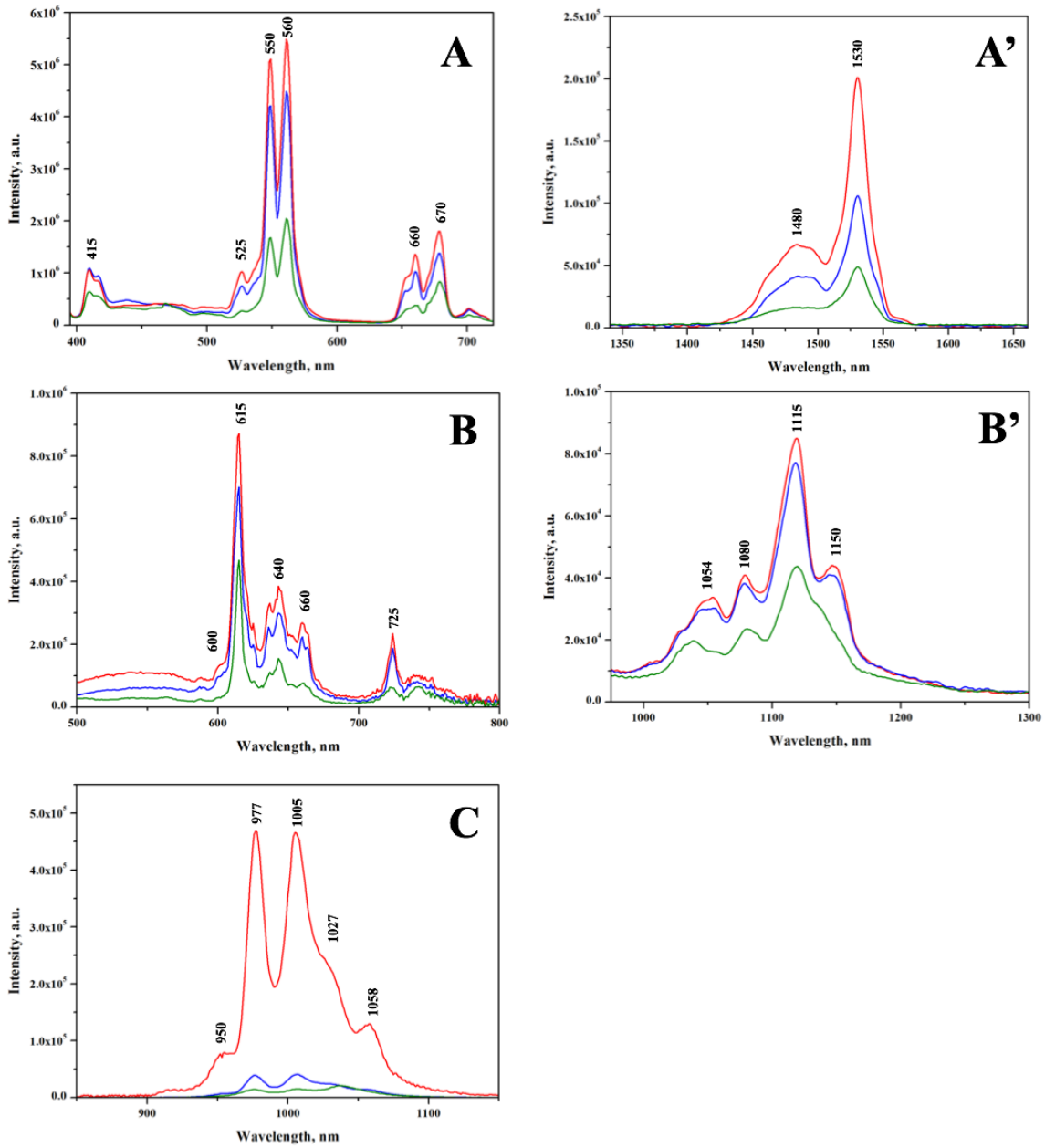

Figure 3 Visible and NIR emission spectra **A, A'** Er:ZrO_2 samples; **B, B'** $PrZrO_2$ samples; **C**: Yb:ZrO_2 samples at increasing dopant concentrations: 1% (red curves); 2% (blue curves) and 10% (green curves)

The five peaks in NIR emission spectra of Yb:ZrO_2 are associated to the transitions from the lowest sublevel of excited multiplet $^2F_{5/2}$ to the sublevels of ground multiplet $^2F_{7/2}$.[29] In particular, the most intense signals centred at 977 nm and 1005 nm are assigned to the transition from the sublevel 5 of the excited state $^2F_{5/2}$ to the level 1 and 2 of the ground state $^2F_{7/2}$, respectively.

Table 3 Assignment of the emission of Er^{3+}, Pr^{3+} and Yb^{3+} transitions observed in fluorescence spectra

Ln^{3+} ion	λ_{exc} [nm]	λ_{em} [nm]	f-f transitions
Er^{3+}	377	415	$^2H_{9/2} \rightarrow {}^4I_{15/2}$
		525	$^2H_{11/2} \rightarrow {}^4I_{15/2}$
		550-560	$^4S_{3/2} \rightarrow {}^4I_{15/2}$
		660-670	$^4F_{9/2} \rightarrow {}^4I_{15/2}$
	653	1400-1600	$^4I_{13/2} \rightarrow {}^4I_{15/2}$
Pr^{3+}	450	600-630	$^1D_2 \rightarrow {}^3H_4 + {}^3P_0 \rightarrow {}^3H_6$
		640	$^3P_1 \rightarrow {}^3F_2$
		660	$^3P_0 \rightarrow {}^3F_2$
		725	$^3P_0 \rightarrow {}^3F_4$
		1115	$^1D_2 \rightarrow {}^3F_3 + {}^1D_2 \rightarrow {}^3F_4$
Yb^{3+}	912	930-1200	$^2F_{5/2} \rightarrow {}^2F_{7/2}$

In order to use Ln:ZrO_2 as contrast agent for optical imaging, the results obtained with the luminescence spectroscopy has allowed the selection of the lowest-doping lanthanide samples EZ1, PZ1 and YZ1 for the subsequent functionalization to introduce the therapeutic agent. The low loading of lanthanide dopant, in fact, ensures the maintenance of the size, phase and morphology of pristine ZrO_2 nanoparticles and leads to the best performances in term of the overall luminescence properties.

2.2. Functionalization of EZ1, PZ1 and YZ1

A surface modification of Ln:ZrO_2 nanoparticles is necessary to introduce an additional chemical functionality. The deposition of a non-porous silica shell with amino groups onto EZ1, PZ1 and YZ1 nanoparticles (EZ1@SiO_2, PZ1@SiO_2 and YZ1@SiO_2) has been chosen as a simple method to introduce surface functionality (-NH_2 groups) to covalently bound a photosensitizer (PS) molecules such as Rose Bengal by amide bond formation (**Scheme 1**).

Scheme 1 Functionalization of the Ln:ZrO_2 nanoparticles through the deposition of an aminopropyl-functionalized silica shell and subsequent covalent immobilization of Rose Bengal.

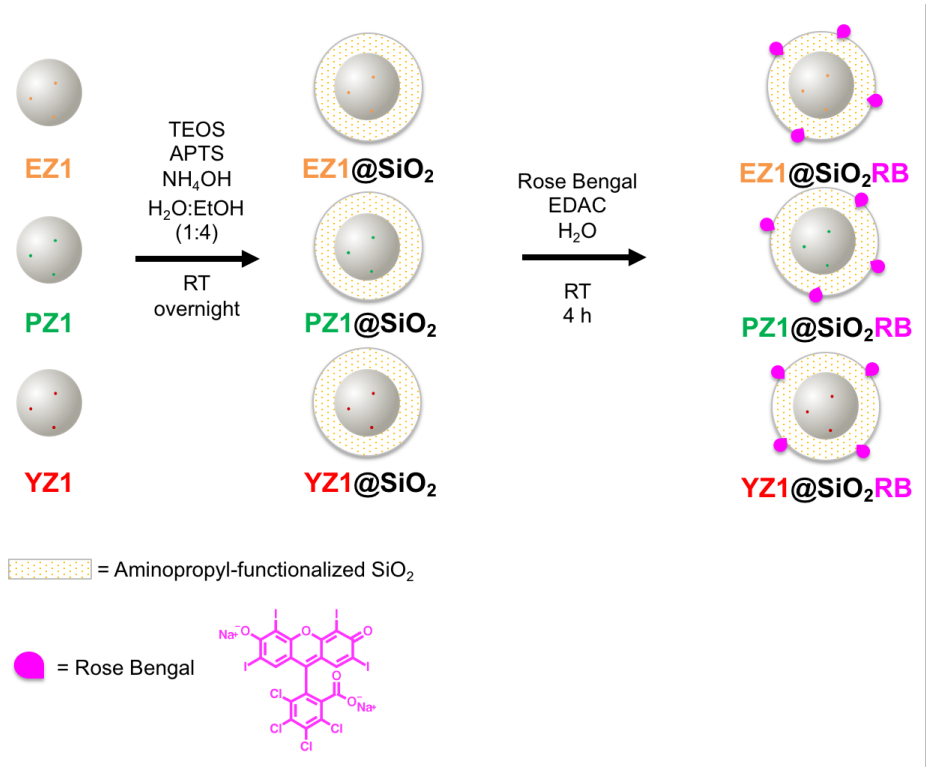

The presence of the silica shell was confirmed by Transmission Electron Microscopy (TEM) and the surface features of the silica-coated nanoparticles before and after the photosensitizer anchoring were assessed by FTIR spectroscopy analysis. In **Figure 4** representative TEM images of the silica coated EZ1 nanoparticles and the corresponding FTIR spectra, collected before and after the anchoring of the photosensitizer, are reported. EZ1 particles appeared to be uniformly coated by a ca. 20-25 nm thick silica shell (figure 4A); neither uncoated ZrO_2 nanoparticles nor free silica nanoparticles were found, indicating that the applied procedure was successful.

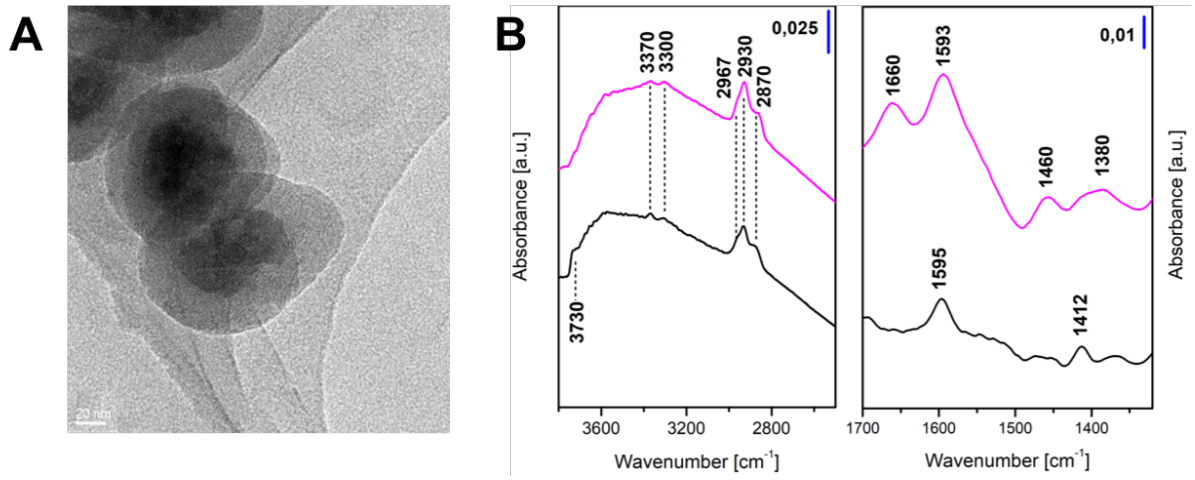

Figure 4 A. Representative TEM image of silica coated EZ1@SiO_2 sample; **B.** FTIR spectra of silica coated EZ1@SiO_2 sample before (black curve) and after (pink curve) the anchoring of Rose Bengal (EZ1@SiO_2RB).

The FTIR spectrum on the silica coated sample, recorded after outgassing the sample at room temperature for 1 hour (**Figure 4B**, black curve), is characterized by signals at 2967, 2930 and 2870 cm^{-1}, ascribed to stretching modes of the CH_2 groups of the aminopropyl chain and CH_3 groups of not completely hydrolysed alkoxy groups. The presence of free amino groups is confirmed by the signals at 3370 and 3300 cm^{-1}, due to the symmetric and asymmetric stretching of NH_2 groups; the corresponding bending mode is visible at 1595 cm^{-1}.

Rose Bengal (RB) was covalently anchored to free amino groups exposed on the surface of EZ1@SiO_2, PZ1@SiO_2 and YZ1@SiO_2. The anchoring of RB to amino groups was confirmed by the presence of the band at 1380-1390 cm^{-1} due to the C-N stretching mode of amide II [30] and the bands at 1660 and 1593 cm^{-1} due to the C=O stretching and N-H bending modes, respectively, in the FTIR spectrum reported in **Figure 4B** (pink curve).

Visible and NIR emission spectra of Ln@SiO_2 and Ln@SiO_2RB samples are reported in **Figure 5**. In the Vis emission spectra of EZ1@SiO_2 (Figure 5A), the typical bands of Er^{3+} can be found at 415 nm, 525 nm, 548 nm, 560 nm, 660 nm and 675 nm. In the case of the EZ1@SiO_2RB sample, the signals are partially covered by the emission band of RB, which is centred at ca. 580 nm, with a bathochromic shoulder at 620 nm. It is worth noting that the

emission spectrum of RB is not significantly perturbed after the anchoring onto EZ1@SiO_2; in fact, the position and maximum-to-shoulder intensity ratio of the emission spectrum of EZ1@SiO_2RB are very close to those of the spectrum of diluted RB solution. This is an indication of the uniform distribution of RB on the silica surface, with a low degree of aggregation. As expected, NIR emission spectra (Figure 5A') are not perturbed neither by the deposition of the silica shell nor by the anchoring of the PS, which has no emission in the NIR region of the spectrum.

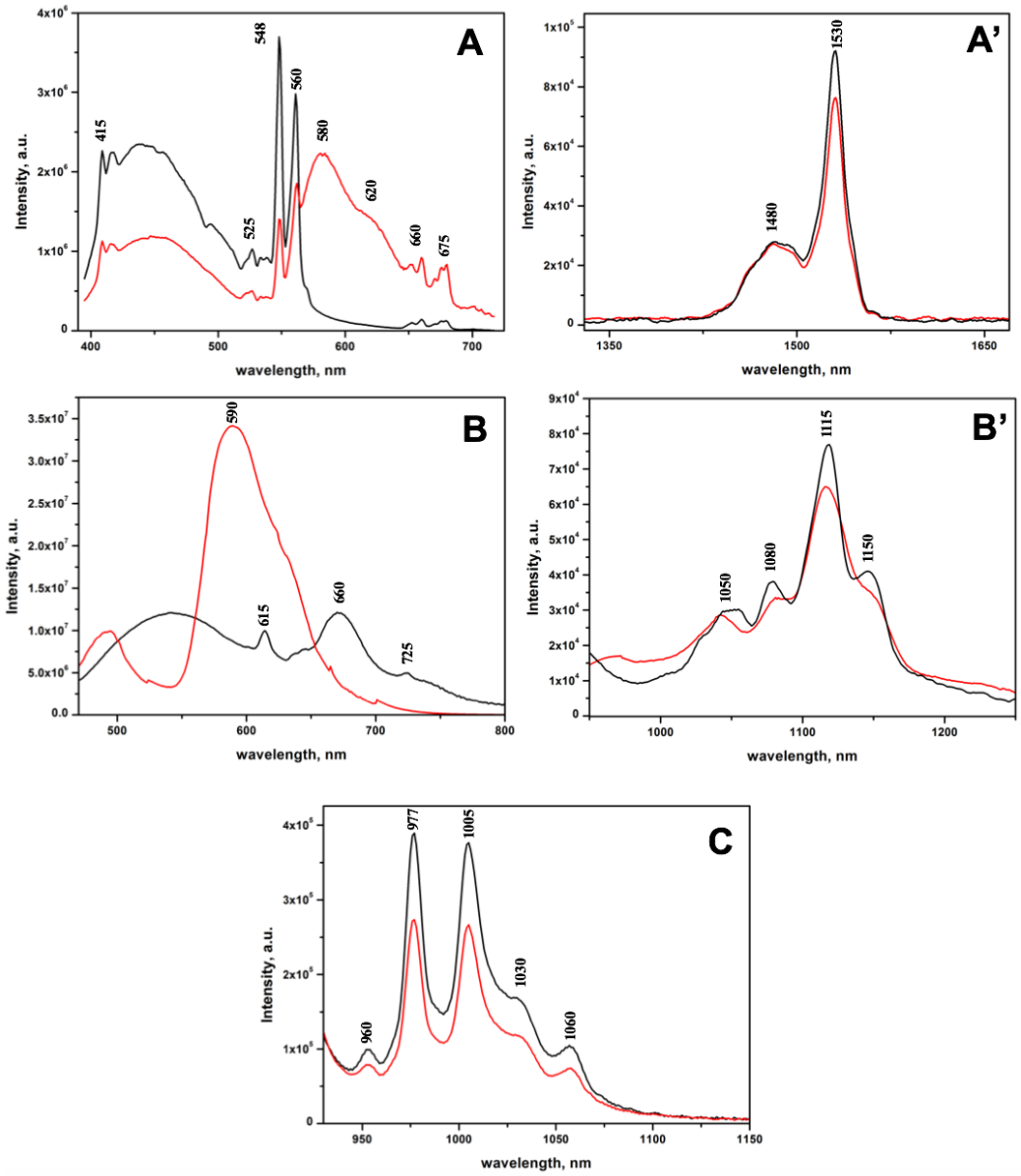

Figure 5 Visible and NIR emission spectra of **A, A'** Er:ZrO_2 samples; **B, B'** PrZrO_2 samples; **C**: Yb:ZrO_2 samples (black curves: silica coated samples; red curves: RB modified samples)

In Figure 5 B and B' visible and NIR emission spectra of PZ1@SiO_2 and PZ1@SiO_2RB are reported. Also in this case, the visible emission spectrum of PZ1@SiO_2RB is dominated by the intense absorption band of RB, whilst the NIR emission spectra appeared to be unperturbed by the deposition of the silica shell and the subsequent anchoring of the photosensitizer. Finally, in Figure 5C the NIR emission spectra of functionalized YZ1 samples are reported; no influence of the silica shell deposition or of the anchoring of RB on the photoemission properties were detected.

2.3. Evaluation of Singlet Oxygen production

A comparative evaluation of the $^1O_2$ release ability of the three nanoplatforms was carried out by an indirect chemical method, using 1,3-diphenylisobenzofuran (DPBF) as scavenger molecule.[31] DPBF, in fact, rapidly reacts with $^1O_2$ forming the colourless o-dibenzoylbenzene derivative. The $^1O_2$ scavenger activity can be monitored through a decrease in the electronic absorption band of DPBF at 411 nm upon illumination for increasing time at 520 nm (**Figure 6**). Irradiation of the pristine lanthanide doped ZrO_2 nanoparticles and of the correspondent silica coated samples (**Figure S4,** supplementary information) does not cause an alteration in the DPBF band, as expected, whilst all the three RB-functionalized samples possess very high $^1O_2$ generation ability.

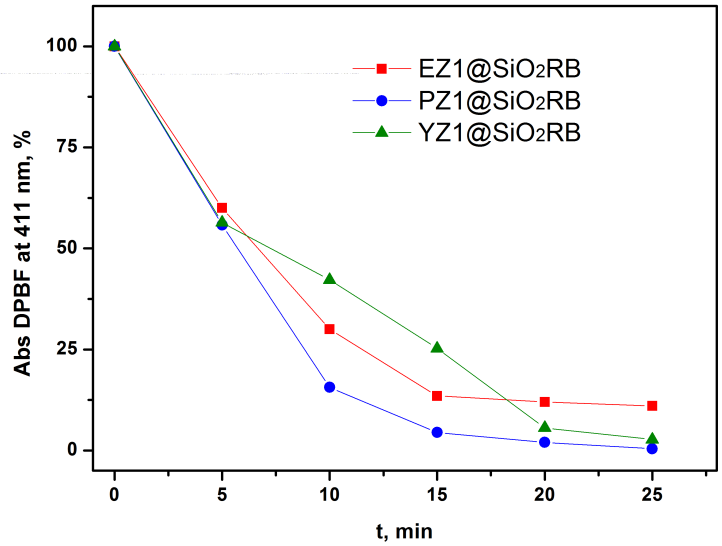

Figure 6 Decrease of the absorption band at 411 nm of DPBF as a function of the irradiation time in presence of EZ1@SiO_2-RB, PZ1@SiO_2-RB and YZ1@SiO_2-RB.

The production of singlet oxygen was also evaluated by the spin trapping technique, using 2,2,6,6-Tetramethyl-4-piperidone (TEMP) as spin trap; the latter reacts with $^1O_2$ released in solution to form the stable nitroxide radical 4-oxo-TEMPO radical adduct, which has a typical EPR signal. All the experiments performed in dark condition did not led to the formation of any detectable radical species. When the experiment was performed under irradiation only the samples containing RB led to the formation of the 4-oxo-TEMPO radical. For all samples the maximum signal intensity was achieved after 60 minutes of irradiation. To evaluate the singlet oxygen production, a double integration of the spectra was performed, since the integrated intensities of the EPR signal are proportional to the number of spins (radicals). The integrated intensities are reported in **Figure 7** as a function of irradiation time.

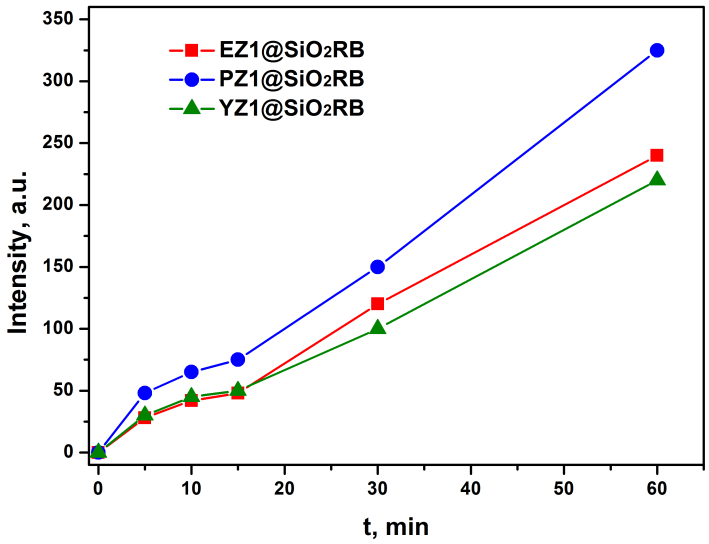

Figure 7 Integrated intensities of the EPR signal as a function of time

2.4. Preliminary cell test

In order to test the potential cytotoxicity of lanthanide doped ZrO_2 nanoparticles as such and after functionalization, the effects of increasing EZ01 or EZ01@SiO2-RB concentrations (0-500 µg/mL) on HeLa cells viability were explored by using the Crystal Violet (CV) assays. No toxicity was observed up to a dose higher than 500 µg/mL (data not shown). Moreover, as the RB-functionalized samples released singlet oxygen upon irradiation, the same samples were tested in vitro for their photodynamic activity. Briefly, HeLa cells were treated for 4h in absence of foetal bovine serum (FBS) with 25µg or 50µg of EZ01 or EZ01@SiO_2-RB, followed by illumination for 5 or 10 minutes and 20h of recovery in presence of FBS. As expected, no significant effect on cell viability was exerted by EZ01, neither illuminated nor in dark conditions. Interestingly, both EZ01@SiO_2-RB concentrations were able to significantly reduce cell viability under light exposure, with respect to control condition (CTRL) and not illuminated condition (-) (**Figure 8**), thus confirming the high potential of these nanoparticles as PDT tools.

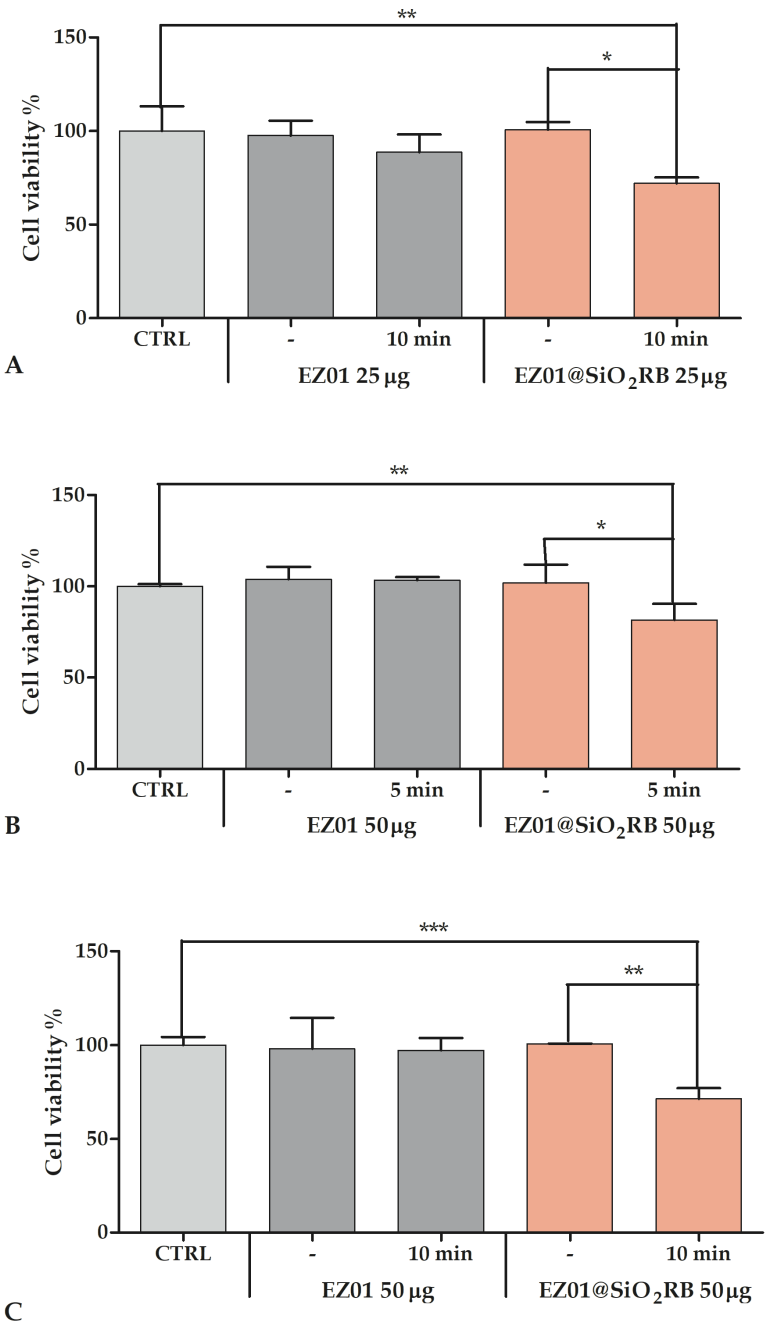

Figure 8 Cell viability after **A** 4h treatment in absence of FBS with 25µg of EZ01 or EZ01@SiO_2RB, followed by illumination for 10 minute, and 20h of recovery in presence of FBS (**p<0.01, *p<0.05); **B** 4h treatment in absence of FBS with 50µg of EZ01 or EZ01@SiO_2RB, followed by illumination for 5 minute, and 20h of recovery in presence of FBS (**p<0.05, *p<0.1); **C** 4h treatment in absence of FBS with 50µg of EZ01 or EZ01@SiO_2RB, followed by illumination for 10 minute, and 20h of recovery in presence of FBS (***p<0.001, **p<0.05)

3. Conclusions

Smart Ln:ZrO_2@SiO_2 nanoplatforms with grafted photosensitizer (Rose Bengal) have been developed to couple optical imaging with photo-dynamic therapy (PDT). A careful control of the lanthanide dopant loading was considered to enhance the photoemission properties of the lanthanide ions (Er, Pr, Yb) inside the ZrO_2 crystal structure.

Among all the samples synthesized, the nanosystems with lowest Ln loading have evidenced high emission intensities in the Vis and NIR region. In addition, upon subsequent functionalization with a silica shell to covalently bound Rose Bengal, a theranostic platform has been obtained and the efficiency in the delivery of singlet oxygen, the cytotoxic agent, have been proved by spin trapping EPR and UV-Vis spectroscopies. Preliminary cell viability tests have evidenced that both pristine and Ln doped ZrO_2 nanoparticles are not cytotoxic, neither upon illumination nor in dark condition. On the contrary, Rose Bengal grafted samples are able to significantly reduce cell viability under light exposure, thus confirming the high potential of these nanoparticles as PDT tools.

4. Experimental Section

Materials. All the reagents and solvents were purchased by Sigma Aldrich (Milano, Italy) and used as received unless otherwise specified.

Synthesis of lanthanide-doped ZrO_2 nanoparticles (Ln:ZrO_2). The samples were prepared via a hydrothermal process starting from a 1.0 M aqueous solution containing the stoichiometric ratio of $ZrOCl_2 \cdot 8H_2O$ and the Ln precursor ($Er(NO_3)_3 \cdot 5H_2O$; $Pr(NO_3)_3 \cdot 6H_2O$; $Yb(NO_3)_3 \cdot 5H_2O$). The pH was then adjusted to 11 using a 4.0 M NaOH aqueous solution, inducing the formation of a gel. The gel was then transferred into a 125 mL Teflon-lined stainless-steel acid digestor, 70% filled, which was heated in oven at 448 K overnight. The precipitates were then centrifuged and washed several times, then dried at 333 K. For comparison pure ZrO_2 was prepared with the same procedure. For each Ln dopant, samples of different concentrations, namely 1%, 2% and 10% molar, were prepared.

Deposition of non-porous silica shell onto lanthanide-doped ZrO_2 nanoparticles (Ln:ZrO_2@SiO_2). The deposition of a non-porous silica layer onto the lanthanide-doped ZrO_2 nanoparticles was performed according to literature procedures.[32] 0.5 g of Ln:ZrO_2 were first suspended in 250 ml of a 1:4 distilled water:absolute ethanol mixture, then 2.5 ml of ammonium hydroxide solution (28-30%) were added to the suspension, following by the dropwise addition of 500µl of Tetraethylorthosilicate (TEOS) as the main silicon source and 50 µl of aminopropyltriethoxysilane (APTES) as the source of functional groups for the covalent conjugation of the photosensitizer. The reaction mixture was stirred at room temperature for 6 hours. The solid product was recovered by centrifugation (10 minutes at 8000 rpm) and washed twice with distilled water.

Covalent conjugation of Rose Bengal (RB) on the surface of Ln:ZrO_2@SiO_2. 0.3 g of the Ln:ZrO_2@SiO_2 material were first suspended in 50 ml of distilled water, then 100 µl of a 3M solution of RB in dimethylformamide (DMF) were added along with 100 µl of a 0.12M solution of N-(3-Dimethylaminopropyl)-N′-ethyl carbodiimide hydrochloride (EDAC) in distilled water. The reaction mixture was stirred at room temperature in the dark for 4 hours, then the solid product was recovered by centrifugation and washed twice with distilled water.

Characterization. XRD patterns were obtained using an ARL XTRA48 diffractometer with Cu Kα radiation (λ = 1.54062 Å). Energy dispersive X-ray (EDX) spectroscopy analysis were carried out on a FEG-SEM TESCAN S9000G instrument equipped with Oxford microanalysis detector Ultim Max and AZTEC Software. Transmission Electron Microscopy (TEM) images were collected on a JEOL 3010 High Resolution Transmission Electron Microscope operating at 300 kV. Specimens were prepared by dispersing the sample by sonication in isopropanol and by depositing a few drops of the suspension on carbon-coated grids. Dynamic Light Scattering (DLS) experiments were performed at 25°C on aqueous MSNs dispersions using Malvern Zetasizer Nano-ZS Instrument, which uses a 4mW He-Ne laser operating at 633 nm and a detection angle of 173°. Suspensions of 0.5 mg mL^{-1} of each material were prepared and

measured immediately after ultrasonication for 15 minutes. Hydrodynamic diameters were obtained from the Intensity-weighted size distribution curve. FTIR spectra of self-supporting pellets were collected under vacuum conditions (residual pressure $<10^{-5}$ Torr) using a Bruker Equinox 55 spectrometer equipped with a pyroelectric detector (DTGS type) with a resolution of 4 cm^{-1}. UV-Vis absorption spectra and DR UV-Vis-NIR spectra were recorded using a Perkin Elmer Lambda 900 spectrometer equipped with a diffuse reflectance sphere attachment. Photoemission and excitation steady state spectra were acquired with a Horiba Scientific Fluorolog spectrofluorimeter equipped with a 450 W Xenon lamp and two detectors: a Hamamatsu R928 photomultiplier for the measurements in the visible range of the spectrum and a LN cooled InGaAs photodiode for measurements in the NIR region. The spectral response was corrected for the spectral sensitivity of the detector.

Determination of Singlet Oxygen generation. 1,3-diphenylisobenzofuran (DPBF) was used as scavenger molecule to evaluate singlet oxygen generation, in fact DPBF rapidly reacts with $^1O_2$ forming the colourless o-dibenzoylbenzene derivative. The $^1O_2$ scavenger activity can be monitored through a decrease in the electronic absorption band of DBPF at 411 nm. A solution of DPBF (20 μM) was added to suspensions of the RB-functionalized samples in water and the final suspension was irradiated with a light source at 520 nm (450 W Xenon Lamp). After fixed time intervals, absorption spectra were collected on a Perkin Elmer Lambda 900 instrument. The decrease DBPF absorption contribution at 411 nm was plotted as a function of the irradiation time. The production of singlet oxygen was also evaluated by the spin trapping technique, using 2,2,6,6-Tetramethyl-4-piperidone (TEMP) as spin probe. The spin probe reacts with the $^1O_2$ to form the stable nitroxide radical 4-oxo-TEMPO, which has a fingerprint ESR signal. 20mg of powder were suspended with 1000μL of MilliQ water. Then, 250μL of a 0.15M TEMP solution were added. The suspension was irradiated with a 500W Xe lamp (Oriel instruments) equipped with a water IR filter and a 495nm cut-off filter. As negative control all

experiments were repeated in dark, without irradiation. Spectra of 50µL of suspension were monitored at 0, 5, 10, 15, 30 and 60 minutes of irradiation.

Cell Culture. HeLa cells, a cervical cancer cell line, were grown at 37°C, 5% CO_2, in DMEM supplemented [33] with 10% foetal bovine serum (FBS) and 1% antibiotic mixture.

Crystal Violet (CV) assay. Cell viability was assessed by staining cells with the CV dye. Cells were settled overnight (20000 cells/well) and then incubated with increasing concentration of EZ01 or EZ01@SiO_2RB (range 0-500 µg/mL) for 4h in absence of FBS. After 20h of recovery in presence of FBS, the medium was then removed, cells were gently washed once with PBS, stained for 10 min with 0.5% CV in 145 mmol/L NaCl, 0.5% formal saline, 50% ethanol, and washed thrice with water. CV was eluted from cells with 33% acetic acid. Plates were read at 540 nm in a plate reader (Infinite 200 Pro, Tecan).[33] Successively cells were treated for 4h in absence of FBS with 25µg or 50µg of EZ01 or EZ01@SiO_2RB, followed by illumination for 5 or 10 minutes. After 20h of recovery in presence of FBS cell viability was assessed by staining with the CV dye as previous described.

Statistical analysis. Data were analyzed with the Instat software package (GraphPad Software) by 1way ANOVA followed by Bonferroni post-test.

Conflicts of Interest: The authors declare no conflicts of interest

Acknowledgements

The FEG-SEM S9000 by Tescan was purchased with funds from Regione Piemonte (project POR FESR 2014-20 INFRA-P SAX).

References

[1] Z. Zhao, J. Yuan, X. Zhao, A. Bandla, N.V. Thakor, M. C. Tan, *ACS Biomater. Sci. Eng.* 2019, **5**, 4089

[2] X. Song, S. Li, H. Guo,W. You, X. Shang, R. Li, D. Tu,W. Zheng, Z. Chen, H. Yang, X. Chen, *Angew.Chem.Int.Ed.* 2019, **58**, 18981

[3] J. Wang, Y. Zhu, C. A. Grimes, Q. Cai, *Nanoscale*, 2019, **11**, 12497

[4] a. Y. Wang, S. Song, S. Zhang, H. Zhang, *Nano Today* 2019, **25**,38. b. Z. Chen, W. Zheng, P. Huang, D. Tu, S. Zhou, M. Huang, X. Chen. *Nanoscale* 2015, **7**, 4274

[5] a. M. Kermorgant, J. Ben Salem, J. Santelli, D. Calise, A-C. Oster, O. Lairez, C. Coudret, M. Verelst, C. Gales, J-M. Sénard, F. Beaudry, A. Pavy-Le Traon, C. Roux, R. Mauricot, D. N. Arvanitis, *PLoS ONE* 2019, **14** (12), e0225729. b. Y. Liu, D. Tu, H. Zhu, E. Ma, X. Chen, *Nanoscale* 2013, **5**, 1369

[6] V. Caratto, F. Locardi, G.A. Costa, R. Masini, M. Fasoli, L. Panzeri, M. Martini, E. Bottinelli, E. Gianotti, I. Miletto, *ACS Appl. Mater. Interf*. 2014, **6**(20),17346

[7] F. Locardi, E. Gianotti, I. Nelli, V. Caratto, A. Martinelli, M. Ferretti, G.A. Costa L. Canesi, T. Balbi, M. Fasoli, M. Martini, B. Martins Estevão, I. Miletto, *Mater. Res. Bull.* 2017, **86**, 220

[8] G. Chen, H. Qiu, P. N. Prasad, X. Chen, *Chem. Rev*. 2014, **114**, 5161

[9] a. S. Kalaivani, S. Kannan, *Dalton Trans*. 2019, **48**, 9291. b. K. Smits, D. Olsteins, A. Zolotarjovs, K. Laganovska, D. Millers, R Ignatans, J Grabis, *Scientific Reports,* 2017*,* **7**, 44453

[10] a. K. Srigurunathan, R. Meenambal, A. Guleria, D. Kumar, J. M. da Fonte Ferreira, S. Kannan, *ACS Biomater. Sci. Eng.* 2019, **5** (4), 1725. b. Y. Liu, S. Zhou, D. Tu, Z. Chen, M. Huang, H. Zhu, E. Ma, X. Chen, *J. Am. Chem. Soc.* 2012, **134**, 15083

[11] J. Zhou, N. Shirahata, H. T. Sun, B. Ghosh, M. Ogawara, Y. Teng, S. Zhou, R. G. Sa Chu, M. Fujii, J. Qiu, *J. Phys. Chem. Lett.* 2013, **4**, 402

[12] U. Rocha, K. U. Kumar, C. Jacinto, I. Villa, F. Sanz-Rodriguez, C. Iglesias de la Cruz Mdel, A. Juarranz, E. Carrasco, F. C. van Veggel, E. Bovero, J. G. Sole, D. Jaque, *Small*, 2014, **10**, 1141

[13] Z. Yan, Z. Wang, Z. Miao, Y. Liu, *Anal. Chem*. 2016, **88**, 922

[14] J-N. Liu, W-B. Bu, J-L. Shi, *Acc. Chem. Res*. 2015, **48**, 1797

[15] a. J. Chena , T. Fana , Z. Xiea , Q. Zengb , P. Xuec , T. Zhengd , Y. Chend , X. Luob, H. Zhang, *Biomaterials*, 2020, **237**, 119827. b. Y. Zhang, K. Ren, X. Zhang, Z. Chao, Y. Yang, D. Ye, Z. Dai, Y. Liu, H. Ju, *Biomaterials* 2018, **163**, 55

[16] D. C. Neckers, *J. Photochem. Photobiol. A* 1989, **47**, 1

[17] E. Gandin, Y. Lion, A. Van der Vorst*, Photochem. Photobiol*. 1983, **37**, 271

[18] R. W. Redmond, J. N. Gamlin, *Photochem. Photobiol*. 1999, **70**, 391

[19] E. Gianotti, B. Martins Estevão, F. Cucinotta, N. Hioka, M. Rizzi, F. Renò, L. Marchese, *Chem. Eur. J*. 2014, **20**, 10921

[20] B. Martins Estevão, F. Cucinotta, N. Hioka, M. Cossi, M. Argeri, G. Paul, L. Marchese, E. Gianotti *Phys. Chem. Chem. Phys.* 2015, **17**, 26804

[21] L. Lutterotti, M. Bortolotti, G. Ischia, I. Lonardelli, H.R.Z. Wenk, *Kristallogr.* 2007, **26**, 125

[22] C. Gionco, M.C. Paganini, E. Giamello, R. Burgess, C. Di Valentin, G. Pacchioni, *Chem. Mater.* 2013, **25**(11), 2243

[23] C. Gionco, M.C. Paganini, E. Giamello, O. Sacco, V. Vaiano, D. Sannino, *J. Energy Chem*. 2017, **26**, 270

[24] W.T. Carnall, *The absorption and fluorescence spectra of rare earth ions in solution* in *Handbook on the Physics and Chemistry of Rare Earths Vol. 3*, Elsevier Science B.V., North-Holland **1979**, pp. 171–208

[25] A. Lukowiak, R. J. Wiglusz, T. Grzyb, M. Ptak, M. Stefanski, A. Chiappini, W. Strek, *J. Alloys Compd*. 2016, **687**, 733

[26] X. Zhang, W. Jiang, H. J. Seo, *Spectr. Lett.* 2015, **48**, 27

[27] Q. Xiao, Q. Zhou, M. Li, *J. Lumin*. 2010, **130**, 1092

[28] L. Del Longo, M. Ferrari, E. Zanghellini, M. Bettinelli, J.A. Capobianco, M. Montagna, F. Rossi, *J. Non-Cryst. Solids* 1998, **231**, 178

[29] H. Wang, Y. Chen, J. Huang, X. Gong, Y. Lin, Z. Luo, Y. Huang, Opt. Express 2014, **22**(18), 21866

[30] K. Liu, X. Liu, Q. Zeng, Y. Zhang, L. Tu, T. Liu, X. Kong, Y. Wang, F. Cao, S.A.G. Lambrechts, M.C.G. Aalders, H. Zhang, *ACS Nano* 2012, **6**, 4054

[31] I. Miletto, A. Fraccarollo, N. Barbero, C. Barolo, M. Cossi, L. Marchese, E. Gianotti, *Dalton Trans*. 2018, **47**, 3038

[32] Y. Wang, B. Li, L.Zhang, P. Li, L. Wang, *Langmuir* 2012, **28**, 1657

[33] E. Ranzato, S. Martinotti, B. Burlando, *J. Ethnopharmacol*. 2011, **134**(2), 443